Multimode Three-Phase *CLLLC* Bidirectional Resonant Converter With Wide Output Voltage Range and Improved Light-Load Efficiency

Tianrui Wang, Qinglin Zhao, Hao Ding, *Member, IEEE*, and Deyu Wang, *Member, IEEE*

***Abstract*—This article proposes a modified three-phase *CLLLC* bidirectional resonant dc-dc converter with wide voltage range and improved light-load efficiency. The converter inherits the advantages of higher power density, lower current ripple, and bidirectional power flow from conventional three-phase *CLLLC* structure. In addition, by employing the newly designed phase-shedding strategy, the converter adds three modes to support precharging and float-charging stages. These features enable the converter to cover all charging stages of the battery. A smooth transition between adjacent operating modes of the converter can be attained. To verify the effectiveness and applicability of the newly designed phase-shielding strategy, a 3.3 kW experimental prototype is built. In charging stage, the primary side dc bus voltage is maintained at 400 V, and the output voltage range is 150 V–480 V, with a maximum efficiency of up to 98%. Besides, the efficiency increases by about 1% at 30% load, 3% at 20% load, and 14% at 10% load compared to the three-phase interleaved mode. In discharging stage, the input voltage range is 300 V–480 V, with a maximum efficiency of up to 98.1%.**

***Index Terms*—Bidirectional resonant converter, light-load, phase-shedding, three-phase interleaved *CLLLC*, wide voltage range.**

I. Introduction

RECENTLY, batteries have been playing an essential role in energy storage systems and electric vehicles. Conventional unidirectional battery chargers are unable to feed energy back to the power grid. As a result, new bidirectional chargers have received widespread attention [1], [2].

As crucial components of bidirectional chargers, isolated bidirectional dc/dc converters are developing rapidly [3], [4], [5]. Among them, the bidirectional *LLC* resonant converter with simple topology and high efficiency is attracting more attention [6], [7]. However, in backward mode, it necessitates complex control methods to achieve a boost [8]. To endow resonant converters with bidirectional buck/boost capabilities, an increasing number of researchers are starting to focus on the structural improvement of resonant converters. The asymmetric *CLLC* resonant converter, based on the conventional bidirectional *LLC* resonant converter, is studied in [9] and [10] by adding a resonant capacitor to the secondary side. This addition enables the converter to have bidirectional buck/boost operational capability [11], but its parameter design requires too many iterations to optimize. The symmetric bidirectional *CLLLC* resonant converter is developed in [12] and [13], by introducing a set of *LC* resonant networks into the secondary side of the conventional *LLC* converter, which exhibits identical output characteristics in both directions. Besides, it is similar to a conventional *LLC* resonant converter in the voltage gain characteristics and parameter design [13]. Nevertheless, the voltage gain curve of the converter possesses two peaks under heavy load conditions, which makes the parameter design more complicated. The *L-LLC* resonant converter, which adds an auxiliary inductor to the primary side, is studied in [14] and [15], and this addition enables it to have good bidirectional voltage gain regulation ability. However, the addition of the auxiliary inductor will increase the reactive circulation and power losses. Zhang et al. [16] proposed a bidirectional *LCLL* resonant converter, but the asymmetric forward and backward gain curves of the converter complicate the parameter design.

Although the aforementioned converters can achieve bidirectional wide gain power conversion, as single-phase converters, there is still a common problem of large current ripple. To solve the problem, two-phase interleaved and three-phase interleaved *LLC* resonant converters are studied in [17] and [18]. Compared with two-phase resonant converters, three-phase resonant converters have advantages such as self-current sharing among phases, lower output current ripple and current stress, improved thermal distribution, and smaller filter size [19], [20], [21]. Therefore, it is better adapted to high-power applications than single-phase resonant converters and two-phase resonant converters. To achieve the bidirectional operation of three-phase resonant converters, the authors in [22] and [23] proposed the three-phase *CLLLC* bidirectional resonant converter and the three-phase *LLCL* bidirectional resonant converter, respectively.

Since the *LLC* converter primarily relies on frequency modulation to regulate the gain range, its inherent gain range is constrained. As the output current diminishes, simply increasing

Received 26 February 2025; accepted 8 April 2025. Date of publication 14 April 2025; date of current version 30 June 2025. This work was supported in part by the Natural Science Foundation of Hebei under Grant E2023203148 and in part by the Science Research Project of Hebei Education Department under Grant ZD2021101. Recommended for publication by Associate Editor M. (GAE) Amirabadi. *(Corresponding author: Qinglin Zhao.)*

The authors are with the School of Electrical Engineering, Yanshan University, Qinhuangdao 066004, China, and also with the Key Laboratory of Power Electronics for Energy Conservation and Drive Control of Hebei Province, Qinhuangdao 066004, China (e-mail: wangtr@stumail.ysu.edu.cn; powerzql@ysu.edu.cn; dinghao@ysu.edu.cn; wdy@ysu.edu.cn).

Color versions of one or more figures in this article are available at https://doi.org/10.1109/TPEL.2025.3560232.

Digital Object Identifier 10.1109/TPEL.2025.3560232

the frequency becomes ineffective in achieving gain reduction. Consequently, it is challenging for resonant converters to implement a precharging mode that supplies low voltage and low current to batteries [24]. To further extend the voltage gain range of the conventional three-phase *LLC* resonant converter, the midpoint of the transformer is connected to the reference ground of the dc bus and two rectifier diodes are added to the secondary side in [25], which makes the converter operate in single-phase half-bridge mode. However, when operating in three-phase mode, this converter is equivalent to three half-bridge circuits connected in parallel. Compared with the three-phase interleaved structure, it will generate higher capacitance voltage stress and larger bus current ripple. Besides, it can only achieve buck/boost regulation in the forward direction.

In addition, as the power level decreases, switching losses increasingly become predominant [26]. Compared with conventional single-phase converters, the efficiency of three-phase converters begins to significantly decrease under light load conditions. However, compared with other charging stages, the light-load absorption stage accounts for the majority of the battery charging time [27]. If the light-load efficiency is too low, the energy loss will be significant over time. Thus, to further boost the light-load efficiency of the bidirectional three-phase *CLLC* resonant converter, the authors in [28] designed three different modes for it through phase-shedding strategies. Although the improvement of light-load efficiency is significant, the designed phase-shedding strategies in [28] fail to expand the gain range of the three-phase bidirectional resonant converter.

This article proposes a modified multimode three-phase *CLLLC* bidirectional resonant dc-dc converter, which adopts pulse frequency modulation (PFM), control, and the MOSFETS on the rectifier side can achieve zero voltage switching (ZVS), in the whole operating time, thereby ensuring high efficiency of the proposed converter. The main contributions of this article can be condensed as follows.

1) The proposed modified three-phase *CLLLC* resonant converter inherits the advantages of conventional three-phase interleaved structure. In three-phase mode, it can effectively decrease the current ripples of input and output ports, and the size of filter capacitors can be significantly reduced. Compared with [25], the capacitance voltage stress and bus current ripple of the modified topology are reduced.
2) In this article, a double voltage rectification (DVR) modulation is proposed to improve the light-load efficiency of the charging stage. With the proposed modified topology and newly designed phase-shedding strategies, the converter can achieve four operation modes, adding a low-voltage low-current precharging mode and a new high-voltage low-current float-charging mode, which enables the converter to cover all charging stages of the battery.
3) The proposed phase-shedding strategies are verified on a 3.3 kW three-phase *CLLLC* resonant converter. The converter offers a 150 V–480 V voltage range, a peak efficiency of 98% and a light-load efficiency of 96% at 20% load. These performance metrics surpass state-of-the-art designs. A comparison with the existing converters is presented in Table II of Section V to illustrate the excellent performance of the designed converter.

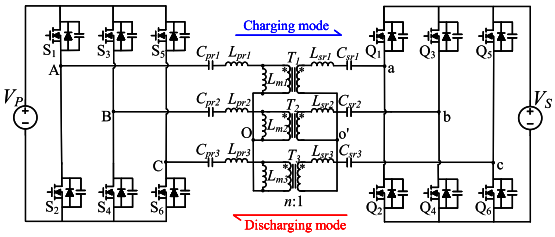

Fig. 1. Conventional three-phase *CLLLC* bidirectional resonant converter.

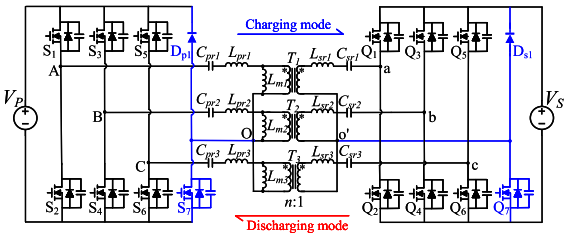

Fig. 2. Proposed modified multimode three-phase *CLLLC* bidirectional resonant converter.

The rest of this article is organized as follows. The operation principle of the proposed converter is introduced in Section II. The voltage gains are derived in Section III. The design methodology and control strategy of the proposed converter are described in Section IV. The experimental results are illustrated in Section V. Finally, Section VI concludes this article.

II. Operation Principle

A. Topology Description

The topology of conventional three-phase *CLLLC* resonant converter is illustrated in Fig. 1. To broaden the gain range and improve the light-load efficiency of conventional three-phase *CLLLC* converter, this article adds a diode and a MOSFETto both sides of it, as shown in Fig. 2.

The voltage at the two dc ports is defined as V_P and V_S, which are, respectively, connected to the dc bus and battery. If the power is transferred from V_P to V_S, the converter works in charging mode, i.e., forward operation; otherwise, it works in discharging mode, i.e., backward operation. This converter has three identical resonant tanks and symmetrical forward and backward voltage gain curves. Therefore, the turns ratio of the three transformers are equal: $n_1 = n_2 = n_3 = n$, and the resonant components satisfy $L_{\rm pr1} = L_{\rm pr2} = L_{\rm pr3} = n^2 L_{sr1} = n^2 L_{sr2} = n^2 L_{sr3} = L_r$, $C_{\rm pr1} = C_{\rm pr2} = C_{\rm pr3} = C_{sr1}/n^2 = C_{sr2}/n^2 = C_{sr3}/n^2 = C_r$, and $L_{m1} = L_{m2} = L_{m3} = L_m$.

When secondary switches are kept OFFand only the body diodes perform their function, this operation is designated as passive rectification (PR). During the charging stage, the proposed modified converter can work in four modes: single-phase half-bridge&PR mode (1P-HB&PR mode) [see Fig. 3(a)], three-phase interleaved&PR mode (3P-IL&PR mode) [see

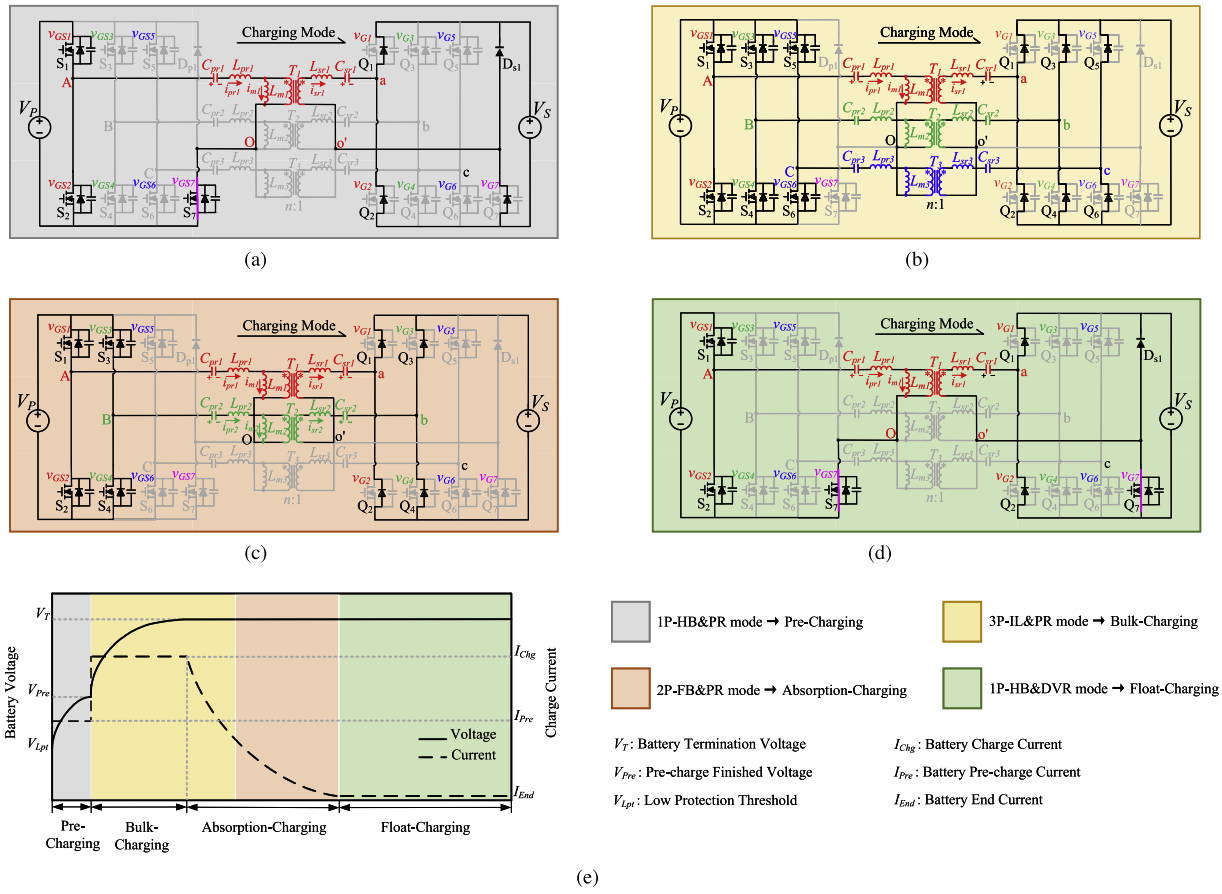

Fig. 3. Proposed phase-shedding strategy for forward charging. (a) 1P-HB&PR mode. (b) 3P-IL&PR mode. (c) 2P-FB&PR mode. (d) 1P-HB&DVR mode. (e) Each mode corresponds to the charging stage.

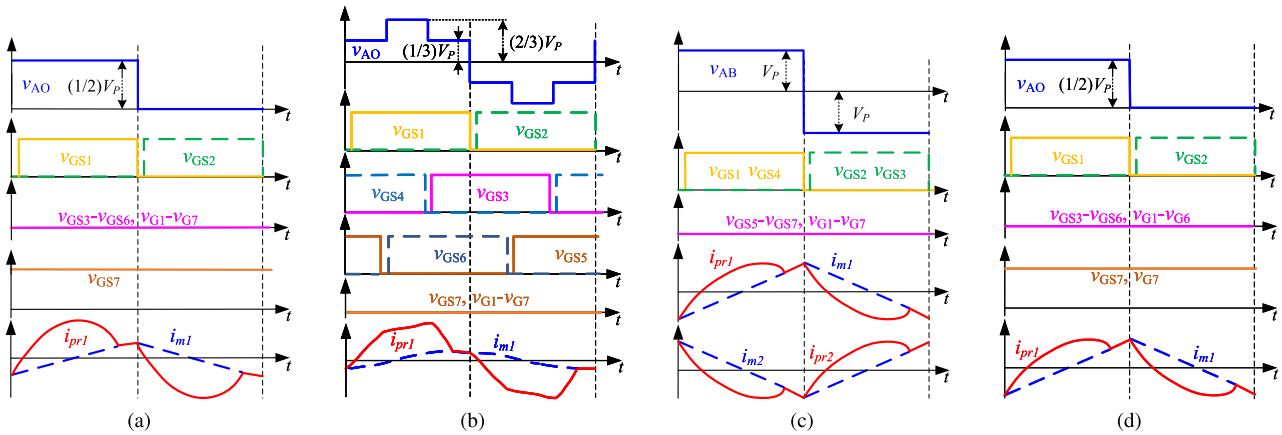

Fig. 4. Principal waveforms. (a) 1P-HB&PR mode. (b) 3P-IL&PR mode. (c) 2P-FB&PR mode. (d) 1P-HB&DVR mode.

Fig. 3(b)], two-phase full-bridge&PR mode (2P-FB&PR mode) [see Fig. 3(c)], and single-phase half-bridge&DVR mode (1P-HB&DVR mode) [see Fig. 3(d)]. Fig. 3(e) shows that the four operating modes can cover all the charging stages of the battery. The principal waveforms during the positive half-cycle of four modes are illustrated in Fig. 4(a)– (d), respectively, where v_{Gs1}–v_{Gs6} are the pulse signals of S_1–S_6, while v_{G1}–v_{G6} are the driving signals of switches Q_1–Q_6. Moreover, v_{ab} represents the resonant tank's input voltage. During the discharging stage, the proposed converter only operates in 3P-IL&PR mode [see Fig. 5(a)].

B. Forward Charging Mode

1) 1P-HB&PR Operation: As shown in Fig. 3(a), the converter works in 1P-HB&PR mode, with S_7 remaining ON, S_1

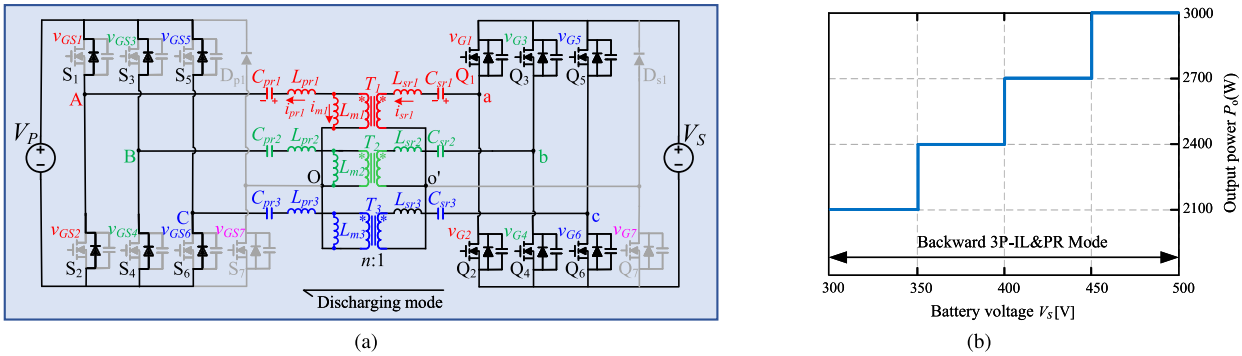

(a) (b)

Fig. 5. Backward discharging mode of the proposed converter. (a) Equivalent circuit. (b) Backward gradient discharge process.

and S_2 complementary conducting with 50% duty ratio, and other switching-legs remaining OFFon the inverter side. The switching-legs, on the rectifier side, remain OFFand perform PR. The principal waveforms are displayed in Fig. 4(a). Owing to the half-bridge operation, the output voltage gain of the converter in the 1P-HB&PR mode is reduced to half compared with that in other modes. Therefore, it can be used for the precharging stage of the battery, providing low voltage and low current during the initial charging stage, thus extending the battery's service life.

2) 3P-IL&PR Operation: In this mode, S_7 remains OFF, while the other legs are shifted by 120° and the upper and lower switches of the same leg conduct complementary with 50% duty ratio on the inverter side. The MOSFETs on the rectifier side function as diodes without receiving driving signals. The corresponding equivalent circuit is shown in Fig. 3(b), and the key waveforms in a switching cycle are shown in Fig. 4(b). In three-phase mode, the current ripple of the output capacitor is substantially reduced. Moreover, it features smaller voltage stress and peak current, and lower conduction losses at higher power levels, thus achieving a higher efficiency. Hence, the 3P-IL&PR mode is utilized to handle the high-power charging stage of the battery.

3) 2P-FB&PR Operation: On the inverter side, S_5, S_6, and S_7 remain OFF, while other switches form a full-bridge circuit, whose resonant tanks can be regarded as in series. On the rectifier side, the switching-legs remain OFF, performing PR. The equivalent circuit is presented in Fig. 3(c) and key waveforms are shown in Fig. 4(c). It should be noted that switch losses dominate under lighter load conditions. Consequently, by shedding one of the phases, lower switch losses and higher efficiency can be achieved compared with the 3P-IL&PR mode. Thus, due to its two-phase structure, the light-load efficiency of the converter can be improved. This mode occupies most of the time in the absorption-charging stage of the battery.

4) 1P-HB&DVR Operation: As shown in Fig. 3(d), the converter works in 1P-HB&DVR mode. On the inverter side, S_7 remains ON, the S_1 and S_2 complementary conduct with 50% duty ratio, and other switching-legs remain OFF, forming a half-bridge circuit. On the rectifier side, a DVR modulation is proposed. This modulation doubles the output voltage to offer a boost voltage gain. During this process, Q_7 remains ON while other switching-legs remain OFF. The key waveforms are displayed in Fig. 4(d). With the newly designed phase-shielding strategy, the 1P-HB&DVR mode further reduces the number of switches and magnetic components, thus improving the light-load efficiency of the converter compared with 2P-FB&PR mode. This mode is expected to cover the floating-charging stage of the battery to provide maximum voltage and a low current.

C. Backward Discharging Mode

On account of the symmetrical structure of the converter, it can also achieve four mode transitions when running in the backward direction. But to protect the battery from excessive discharge, the battery voltage range is limited. Thus, the converter only works in 3P-IL&PR mode. As shown in Fig. 5(a), the switching-legs on the inverter side are shifted by 120°, and the upper and lower switches of the same leg conduct complementarily with 50% duty ratio. The MOSFETs on the rectifier side are used as diodes without driving signals. Due to the symmetrical primary and secondary structure, the forward and backward 3P-IL&PR modes possess the same operational waveforms. Fig. 5(b) shows the change curves of current, voltage, and power during the battery gradient discharge stage when the converter works in backward direction.

III. Voltage Gain Analysis

The first harmonic approximation (FHA) is adopted in this article to analyze the voltage gain of four working modes of the converter. These four modes have the same resonant frequencies as follows:

$$f_r = \frac{1}{2\pi\sqrt{L_{\rm pr}C_{\rm pr}}} = \frac{1}{2\pi\sqrt{L_{sr}C_{sr}}} = \frac{1}{2\pi\sqrt{L_rC_r}}. \quad (1)$$

A. Operation Modes

1) 1P-HB&PR Mode: From Fig. 6(a), it is clear that in the 1P-HB&PR mode, the converter operates as a half-bridge *CLLLC* resonant converter. Since it is equivalent to a half-bridge circuit, the input voltage of the resonant tank is half of the voltage value in the 2P-FB&PR modes. Fig. 6(b) shows the FHA equivalent circuit of 1P-HB&PR mode. This accounts for its lower gain compared to the converter in other modes. Based on the FHA, the input voltage of the resonant tank, denoted as

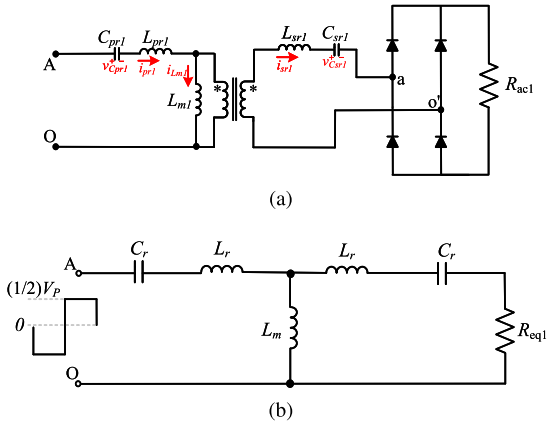

Fig. 6. Equivalent circuit of 1P-HB&PR mode. (a) Equivalent resonant tank circuit. (b) FHA equivalent circuit.

$V_{\mathrm{AO}}(t)$, can be formulated as follows:

$$V_{\mathrm{AO}}(t) = \frac{V_{\mathrm{p}}}{2} + \frac{2V_{\mathrm{p}}}{\pi}\sin\omega t + \frac{2V_{\mathrm{p}}}{3\pi}\sin 3\omega t + \cdots . \tag{2}$$

The voltage gain of the mode can be derived as follows:

$$M_{\text{1P-HB}}(f_n, k, Q_{\text{1P-HB}}) = \frac{1}{2\sqrt{\left(1+\frac{1}{k}-\frac{1}{kf_n^2}\right)^2 + \frac{Q_{\text{1P-HB}}^2}{k^2}\left[(2k+1)f_n - \frac{2(k+1)}{f_n} + \frac{1}{f_n{}^3}\right]^2}} \tag{3}$$

where k is the inductor ratio, f_n is the normalized frequency, f_r is the resonant frequency, Q_{1P-HB} is the quality factor, and Z_{1P-HB} is the characteristic impedance of the 1P-HB&PR circuit as follows:

$$k = \frac{L_m}{L_r}, \quad f_n = \frac{f_s}{f_r}, \quad f_r = \frac{1}{2\pi\sqrt{L_r C_r}}$$

$$Q_{1P-HB} = \frac{Z_{1P-HB}}{R_{eq1}}, Z_{1P-HB} = Z_o = \sqrt{\frac{L_r}{C_r}}. \tag{4}$$

The equivalent ac resistance R_{eq} is as follows:

$$R_{\mathrm{eq1}} = \frac{8}{\pi^2}\cdot R_{L1}\cdot n^2. \tag{5}$$

2) 3P-IL&PR Mode: Since the operating characteristics of each phase are the same in this mode, the gain characteristics of the overall circuit can be analyzed by a single-phase resonant network, as shown in Fig. 7(a). The FHA equivalent circuit is illustrated in Fig. 7(b). According to the Fourier series analysis, the phase voltage $V_{\mathrm{AO}}(t)$ can be formulated as follows:

$$V_{\mathrm{AO}}(t) = \frac{2V_{\mathrm{p}}}{\pi}\sin\omega t + \frac{2V_{\mathrm{p}}}{5\pi}\sin 5\omega t + \cdots \tag{6}$$

The voltage gain of the mode is as follows:

$$M_{\text{3P-IL}}(f_n, k, Q_{\text{3P-IL}}) = \frac{1}{\sqrt{\left(1+\frac{1}{k}-\frac{1}{kf_n^2}\right)^2 + \frac{Q_{\text{3P-IL}}^2}{k^2}\left[(2k+1)f_n - \frac{2(k+1)}{f_n} + \frac{1}{f_n{}^3}\right]^2}} \tag{7}$$

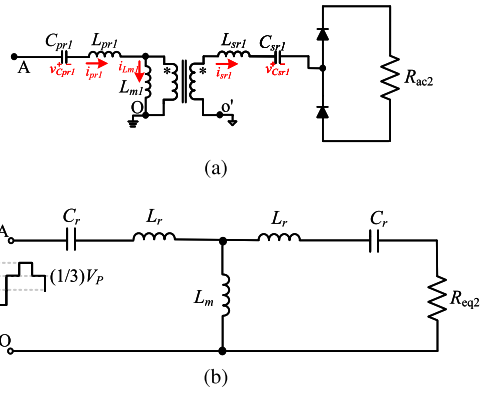

Fig. 7. Equivalent circuit of 3P-IL&PR mode. (a) Equivalent resonant tank circuit of phase-A. (b) FHA equivalent circuit of phase-A.

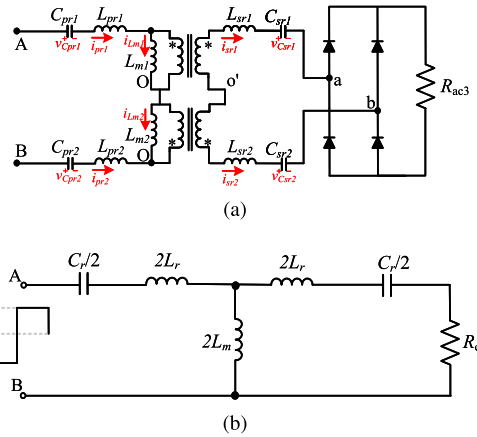

Fig. 8. Equivalent circuit of 2P-FB&PR mode. (a) Equivalent resonant tank circuit. (b) FHA equivalent circuit.

where

$$k = \frac{L_m}{L_r}, f_n = \frac{f_s}{f_r}, Q_{\text{3P-IL}} = \frac{Z_{\text{3P-IL}}}{R_{\text{eq2}}}, f_r = \frac{1}{2\pi\sqrt{L_r C_r}}$$

$$Z_{\text{3P-IL}} = Z_o = \sqrt{\frac{L_r}{C_r}}, R_{\text{eq2}} = \frac{6}{\pi^2}\cdot R_{L2}\cdot n^2. \tag{8}$$

3) 2P-FB&PR Mode: This mode's equivalent circuit possesses doubled excitation inductance and resonant inductance, and the resonant capacitance is halved compared with the other two modes, as shown in Fig. 8(a). The FHA equivalent circuit is illustrated in Fig. 8(b). Thus, the characteristic impedance $Z_{\text{2P-FB}}$ of this mode is twice that of other modes, and under the same equivalent ac resistance, the quality factor Q is twice that of other modes. Although the resonance parameters of the mode have changed, its resonance frequency is the same as the other three modes.

According to the Fourier series analysis, the voltage across the two bridges $V_{\mathrm{AB}}(t)$ can be formulated as follows:

$$V_{\mathrm{AB}}(t) = \frac{4V_{\mathrm{p}}}{\pi}\sin\omega t + \frac{4V_{\mathrm{p}}}{3\pi}\sin 3\omega t + \cdots \tag{9}$$

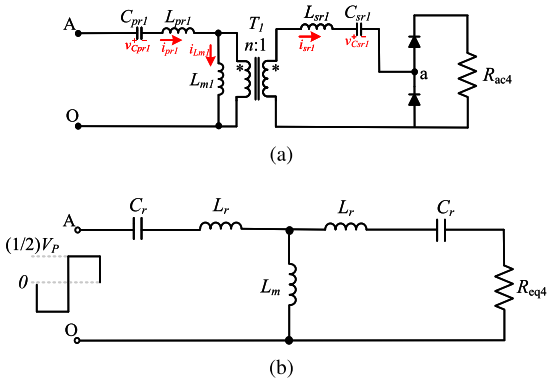

Fig. 9. Equivalent circuit of 1P-HB&DVR mode. (a) Equivalent resonant tank circuit. (b) FHA equivalent circuit.

The voltage gain of the mode is as follows:

$$M_{\text{2P-FB}}(f_n,k,Q_{\text{2P-FB}})=\frac{1}{\sqrt{\left(1+\frac{1}{k}-\frac{1}{kf_n^2}\right)^2+\frac{Q_{\text{F.2p}}^2}{k^2}\left[(2k+1)f_n-\frac{2(k+1)}{f_n}+\frac{1}{{f_n}^3}\right]^2}} \tag{10}$$

where

$$k=\frac{L_m}{L_r},f_n=\frac{f_s}{f_r},Q_{\text{2P-FB}}=\frac{Z_{\text{2P-FB}}}{R_{\text{eq3}}},f_r=\frac{1}{2\pi\sqrt{L_rC_r}}$$

$$Z_{\text{2P-FB}}=2Z_o=2\sqrt{\frac{L_r}{C_r}},R_{\text{eq3}}=\frac{8}{\pi^2}\cdot R_{L3}\cdot n^2. \tag{11}$$

4) 1P-HB&DVR Mode: Though the inverter side is equivalent to the half-bridge circuit, a DVR modulation is proposed on the rectifier side to provide a boost voltage gain, as shown in Fig. 9(a). This accounts for its ability to achieve high voltage output. The FHA equivalent circuit is illustrated in Fig. 9(b). Based on the FHA, the input voltage $V_{\text{AO}}(t)$ can be formulated as follows:

$$V_{\text{AO}}(t)=\frac{V_{\text{P}}}{2}+\frac{2V_{\text{P}}}{\pi}\sin\omega t+\frac{2V_{\text{P}}}{3\pi}\sin 3\omega t+\cdots \tag{12}$$

The voltage gain of the mode can be derived as follows:

$$M_{\text{1P-DVR}}(f_n,k,Q_{\text{1P-DVR}})=\frac{1}{\sqrt{\left(1+\frac{1}{k}-\frac{1}{kf_n^2}\right)^2+\frac{Q_{\text{1P-DVR}}^2}{k^2}\left[(2k+1)f_n-\frac{2(k+1)}{f_n}+\frac{1}{{f_n}^3}\right]^2}} \tag{13}$$

where k is the inductor ratio, f_n is the normalized frequency, f_r is the resonant frequency, $Q_{\text{1P-DVR}}$ is the quality factor, and $Z_{\text{1P-DVR}}$ is the characteristic impedance of the 1P-HB&DVR circuit as follows:

$$k=\frac{L_m}{L_r},\quad f_n=\frac{f_s}{f_r},\quad f_r=\frac{1}{2\pi\sqrt{L_rC_r}}$$

$$Q_{\text{1P-DVR}}=\frac{Z_{\text{1P-DVR}}}{R_{\text{eq4}}},Z_{\text{1P-DVR}}=Z_o=\sqrt{\frac{L_r}{C_r}}. \tag{14}$$

The equivalent ac resistance R_{eq} is as follows:

$$R_{\text{eq4}}=\frac{8}{\pi^2}\cdot R_{L4}\cdot n^2. \tag{15}$$

IV. Design Considerations

According to the voltage gain expressions obtained in Section III, this article conducts a detailed parameter design analysis to ensure continuous voltage gain and achieve ZVS. The design specifications for the proposed converter are summarized as follows:

1) Bus voltage is $V_P=400$ V;
2) Forward output voltage range is $V_S=150$ V–480 V;
3) Backward input voltage range is $V_S=300$ V–480 V;
4) Maximum output power is 3.3 kW;
5) Resonant frequency is $f_r=100$ kHz;
6) Switching frequency range is $f_s=70$ kHz–200 kHz.

A. Analysis of Constraint Condition

For the convenience of design, this article adopts a completely symmetrical bidirectional *CLLLC* resonant structure. The full-load power of the converter is 3.3 kW. When transitioning to the 1P-HB&PR or 2P-FB&PR mode, the maximum power for each phase is restricted to one-third of the full-load power, which is 1.1 kW.

The output voltage range of the converter in forward operation is 150 V–480 V, and the transition voltage of 1P-HB&PR mode to 3P-IL&PR mode is designed to be 270 V. Thus, the voltage range of 1P-HB&PR mode and forward 3P-IL&PR mode is 150 V–270 V and 270 V–480 V, respectively. The 2P-FB&PR mode and 1P-HB&DVR mode operate in the 480 V constant voltage (CV) mode and maintain a low current output.

In the forward 3P-IL&PR mode with a rated current of 6.9 A, when the bus voltage remains at 400 V, the output voltage varies within the range of 270 V–480 V. When the switching frequency coincides with the resonant frequency, the output voltage is set at 400 V, thus the transformer turns ratio $n=1$.

B. Analysis of Forward and Backward Voltage Gain Range

The 2P-FB&PR mode and 1P-HB&DVR mode operate almost at a fixed frequency point. Although (11) shows the Z_F of 2P-FB&PR mode is doubled compared with other modes, it operates in a light load state, resulting in a higher R_{eq} and smaller Q. When the 3P-IL&PR mode can achieve a 480 V gain output, the 2P-FB&PR mode can also achieve it. Therefore, this section mainly analyzes the voltage gain curves of 3P-IL&PR mode and 1P-HB&PR mode.

In forward operation, the minimum gain $M_{\text{F\_min}}$ and maximum gain M_{F_max} of each mode are as follows:

3P-IL&PR mode:

$$M_{\text{F.3p\_min}}=\frac{nV_{\text{S\_min}}}{V_{\text{P}}}=\frac{270}{400}=0.675 \tag{16}$$

$$M_{\text{F.3p\_max}}=\frac{nV_{\text{S\_max}}}{V_{\text{P}}}=\frac{480}{400}=1.2. \tag{17}$$

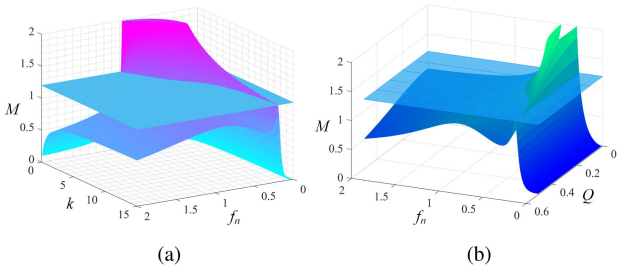

Fig. 10. 3-D gain curves in 3P-IL&PR mode. (a) M_F versus f_n and k. (b) M_F versus f_n and Q_F.

1P-HB&PR mode:

$$M_{\text{F.1p\_min}} = \frac{nV_{\text{S\_min}}}{0.5V_{\text{P}}} = \frac{150}{200} = 0.75 \tag{18}$$

$$M_{\text{F.1p\_max}} = \frac{nV_{\text{S\_max}}}{0.5V_{\text{P}}} = \frac{270}{200} = 1.35. \tag{19}$$

2P-FB&PR mode:

$$M_{\text{F.2p}} = M_{\text{F.3p\_max}} = 1.2. \tag{20}$$

In backward operation, the minimum gain $M_{\text{R\_min}}$ and maximum gain M_{R_max} are as follows:

$$M_{\text{R.3p\_min}} = \frac{V_{\text{P}}}{nV_{\text{S\_max}}} = \frac{400}{480} = 0.83 \tag{21}$$

$$M_{\text{R.3p\_max}} = \frac{V_{\text{P}}}{nV_{\text{S\_min}}} = \frac{400}{300} = 1.33. \tag{22}$$

According to (16), (17), (21), and (22), the voltage gain range of 3P-IL&PR mode is 0.675–1.33. Equations (18) and (19) show that the voltage gain range of 1P-HB&PR mode is 0.7–1.35. Considering the greater voltage gain variation range that the 3P-IL&PR mode withstands, priority is given to the parameter design of the 3P-IL&PR mode.

C. Analysis of Voltage Gain Curves

Due to the symmetrical resonant tank structure and similar working characteristics, the voltage gain curves of the forward and backward 3P-IL&PR modes are identical. Fig. 10(a) illustrates that when the inductor ratio k is too large, there will be two peaks of the converter in 3P-IL&PR mode. In addition, the smaller k is, the wider the voltage gain range is, but too small k will result in high cycle and conduction losses, which will decrease the efficiency of the converter. Therefore, the selection of k requires compromise, and in this article, $k = 5$ is finally chosen.

Fig. 10(b) illustrates that when the quality factor Q is unreasonable, it will result in a nonmonotonic gain curve in the inductive region. To avoid this situation, it is necessary to balance the selection of parameters for 3P-IL&PR mode and 1P-HB&PR mode. Fig. 11 illustrates the effect of different Q on the 3P-IL&PR mode gain curve when $k = 5$. It can be observed that when Q reaches a maximum value of 0.4, the gain curve of the converter can remain monotonic in the inductive region. After determining k, a larger Q should be chosen as far as possible while ensuring ZVS to reduce switch losses. Therefore,

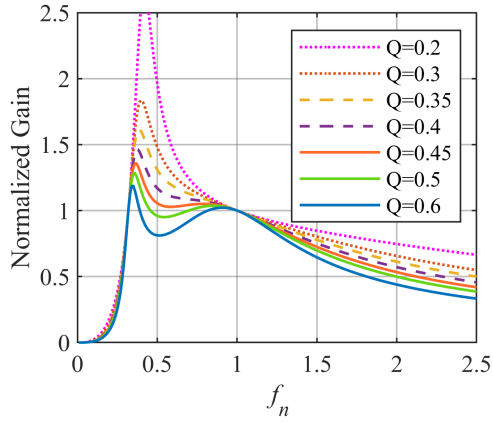

Fig. 11. Voltage gain versus normalized frequency in 3P-IL&PR mode.

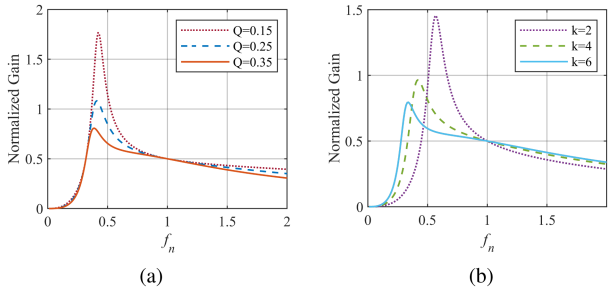

Fig. 12. Voltage gain versus normalized frequency of 1P-HB&PR mode. (a) Effect of Q on gain when $k = 5$. (b) Effect of k on gain when $Q = 0.3$.

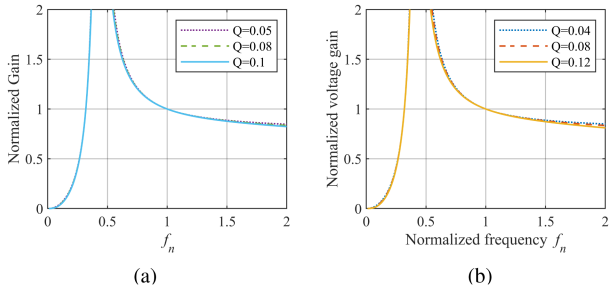

Fig. 13. Voltage gain versus normalized frequency. (a) 2P-FB&PR mode. (b) 1P-HB&DVR mode.

when outputting 270 V/6.6 A in 3P-IL&PR mode, $Q = 0.39$ is selected. According to (8), it can be obtained

$$\begin{cases} R_{L.3p} = U_S/I_S \\ R_{\text{eq.}3p} = 6\pi^2 \cdot R_{L.3p} \cdot n^2 \\ Z_o = Q \cdot R_{\text{eq.}3p}. \end{cases} \tag{23}$$

Then, according to (23), the value of Z_o is calculated. The gain curves of the 1P-HB&PR mode, as shown in Fig. 12, are monotonic in the inductive region. Fig. 13 presents the gain curves of the 2P-FB&PR mode and 1P-HB&DVR mode. And the required gain within reasonable frequency can be achieved of these modes, so the selection of k, Q, and Z_o is feasible.

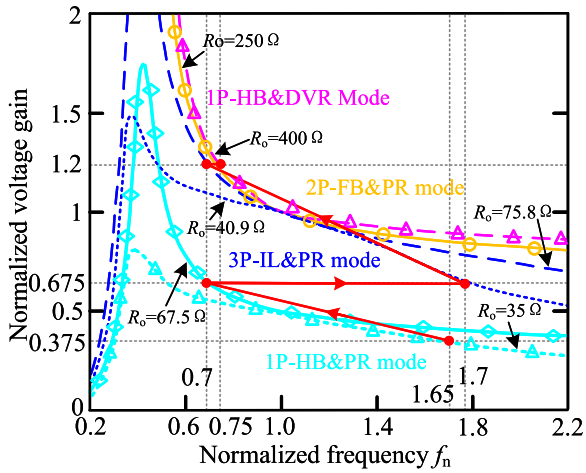

Fig. 14. Voltage gain curves of four modes.

D. ZVS Condition

The dead time of the upper and lower switches on the same leg is set to 200 ns, the parasitic capacitance C_{oss} of the switches is 200 pF, and the resonant frequency f_r is 100 kHz. To ensure the ZVS in all modes, L_m should satisfy the following:

$$L_m < \frac{nU_{S\_\min}t_{\text{dead}}}{8C_{\text{oss}}U_P f_r} \tag{24}$$

where $nU_{S\_\min}/U_P = M_{F\_\min}$

$$L_m < \frac{M_{F\_\min}t_{\text{dead}}}{8C_{\text{oss}}f_r}. \tag{25}$$

According to (16), (18), and (20), $M_{\text{F.3p\_min}} < M_{\text{F.1p\_min}} < M_{\text{F.2p}}$. Therefore, to satisfy the ZVS conduction of switches, a smaller magnetizing inductance L_m is required in 3P-IL&PR mode compared with 1P-HB&PR mode and 2P-FB&PR mode. When the 3P-IL&PR mode satisfies the ZVS condition, alterations to the operation mode have no impact on the realization of ZVS for the switches. The final designed parameters of the resonant tank are $L_r = 15.4$ μH, $L_m = 68$ μH, and $C_r = 164$ nF. After calculation, the designed L_m can achieve ZVS in all modes. According to the selected parameters, the voltage gain curves of four modes and the detailed operation range are illustrated in Fig. 14.

E. Control Design

Taking the forward operation as an example, a dual-loop control scheme is adopted in this article, as shown in Fig. 15. During steady-state operation, the voltage and current loops are calculated separately, with only one control loop running and the other saturated. The smaller calculated value is used as the output to control the switching frequency.

The control flowchart of the proposed converter is illustrated in Fig. 16, where $V_{\text{tran1}} = 270$ V, $I_{\text{tran1}} = 3$ A, and $I_{\text{tran2}} = 1.5$ A. A smooth mode transition strategy based on frequency matching is adopted to ensure stable operation during mode changes. Specifically, before switching to the next mode, all switches are turned OFF within 1–2 switching cycles and the PI controller is disabled.

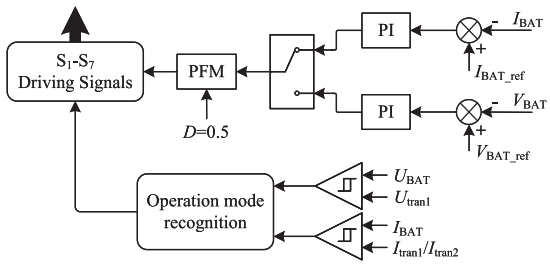

Fig. 15. Control diagram of the proposed converter for forward battery charging.

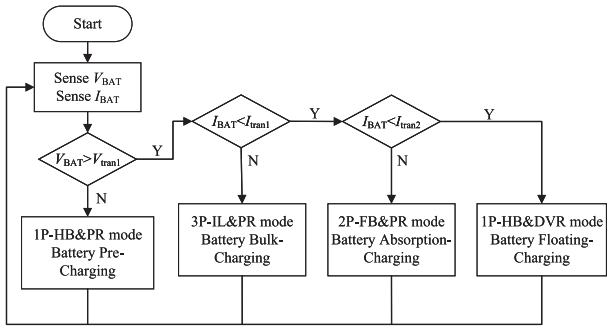

Fig. 16. Control flowchart of the proposed converter for forward battery charging.

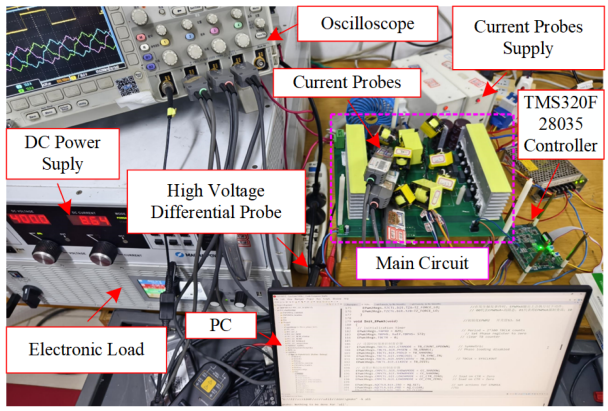

Fig. 17. Experimental prototype of the proposed multimode three-phase *CLLLC* bidirectional resonant converter.

When the switches are turned ON again, it is done according to the control logic of the next mode and the corresponding switching frequency under the desired output voltage. This method can reduce the inrush current and shorten the transition time.

V. Experimental Verification

A 3.3 kW prototype, as shown in Fig. 17, is built to validate the correctness of theoretical analysis. Table I presents the specifications of the experimental platform.

A. Forward Charging Stage

The experimental waveforms during the forward charging stage are presented in Fig. 18. The resonant frequency of the

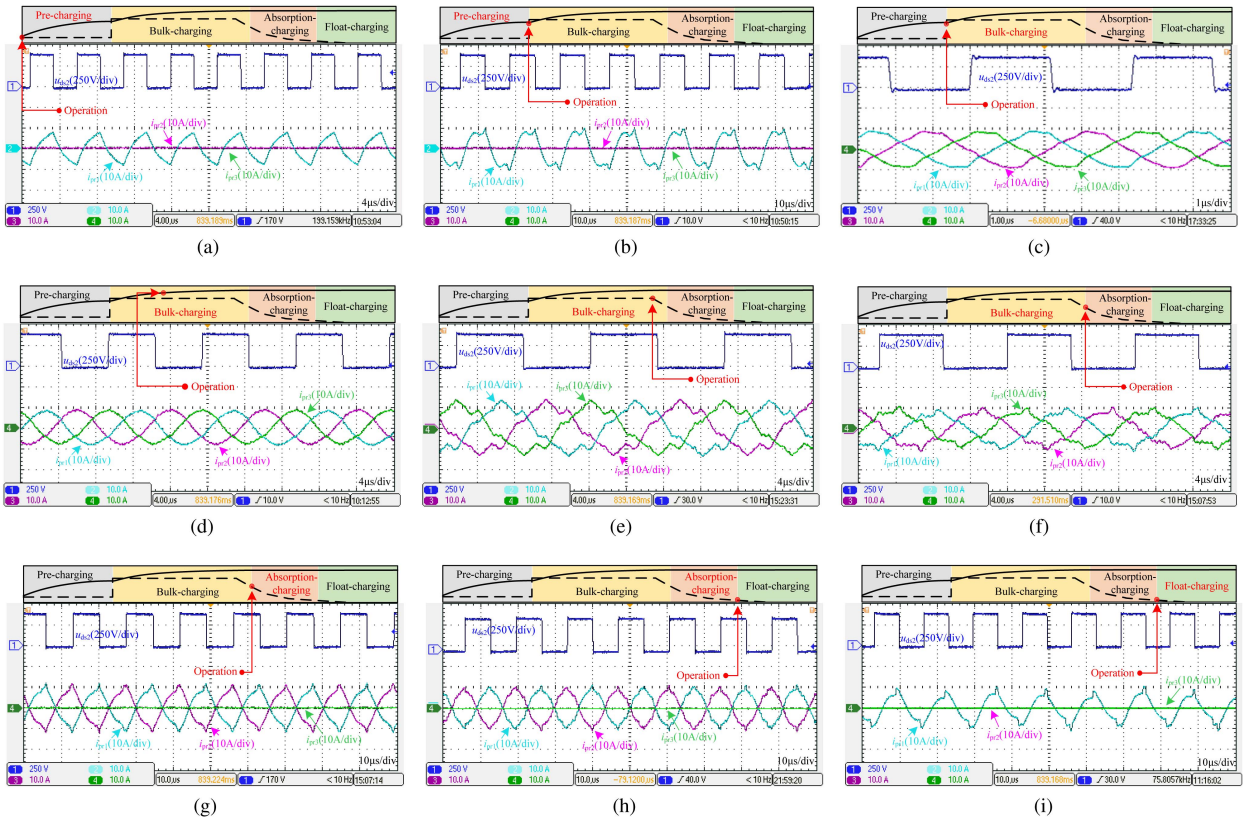

Fig. 18. Experimental waveforms in forward charging operation i_{pr1}, i_{pr2}, i_{pr3}, and u_{ds2}. (a) When output 150 V/4 A in 1P-HB&PR mode. (b) When output 270 V/4 A in 1P-HB&PR mode. (c) When output 270 V/6.9 A in 3P-IL&PR mode. (d) When output 400 V/6.9 A in 3P-IL&PR mode. (e) When output 480 V/6.9 A in 3P-IL&PR mode. (f) When output 480 V/2 A in 3P-IL&PR mode. (g) When output 480 V/2 A in 2P-FB&PR mode. (h) When output 480 V/1 A in 2P-FB&PR mode. (i) When output 480 V/1 A in 1P-HB&DVR mode.

TABLE I
PARAMETERS OF EXPERIMENTAL PLATFORM

Items	Parameters
Resonant frequency f_r	100kHz
Switch frequency f_s	70kHz-220kHz
Resonant inductor L_{pr}, L_{sr}	13.6μH (Ferroxcube PQ26/25)
Resonant capacitance C_{pr}, C_{sr}	182nF (MMKP82)
Magnetizing inductor L_m	68μH (Ferroxcube PQ35/35)
Turns ratio $n = (n_1 : n_2)$	1=(30:30)
Switches S_1-S_7, Q_1-Q_7	IPW60R070CFD7
Diodes D_{p1}, D_{s1}	CI10S65C4I

four modes is 100 kHz. The switching frequency of 3P-IL&PR mode floats between 70 and 220 kHz to adjust the output voltage. The frequency variation range of 1P-HB&PR mode is 70 to 170 kHz. The 2P-FB&PR and 1P-HB&DVR modes operate at around 75 kHz.

1) 1P-HB&PR Mode: This mode is used to expand the voltage gain of the converter to cover the precharging stage. As a single-phase structure, its maximum power is limited to one-third of the three-phase full load power, which is 1.1 kW. Therefore, this mode maintains a constant current (CC) of 4 A output while providing an output voltage range of 150 V–270 V. The experimental results of the 1P-HB&PR mode are shown in Fig. 18(a) and (b), which show that when the converter works in the 1P-HB&PR mode, the other two phases are shed and no current flows.

2) 3P-IL&PR Mode: Compared with 1P-HB&PR or 2P-FB&PR modes, this mode is more suitable for high-power application. This is attributable to the distinctive characteristics offered by the three-phase interleaved structure, which include reduced output current ripple and filter size, smaller peak current value, and lower conduction losses at higher power transfer. The output voltage range of the mode is set to 270 V–480 V. Fig. 18(c)–(f) shows the experimental waveforms of the 3P-IL&PR mode, which indicate that the resonant currents of each phase are balanced and the designed gain of the mode can be achieved.

3) 2P-FB&PR Mode: During the absorption-charging stage, the efficiency provided by the 2P-FB&PR mode is higher than that of the 3P-IL&PR mode. Fig. 18(g) and (h) shows the experimental waveforms of the 2P-FB&PR mode at different powers. The experimental results demonstrate that the 2P-FB&PR mode can cover the absoption-charging stage of the converter with balanced two-phase current.

4) 1P-HB&DVR Mode: In comparison to the 2P-FB&PR mode, the 1P-HB&DVR mode leads to a further reduction in the quantity of switches and magnetic components. As a consequence, the light-load efficiency of the converter is enhanced.

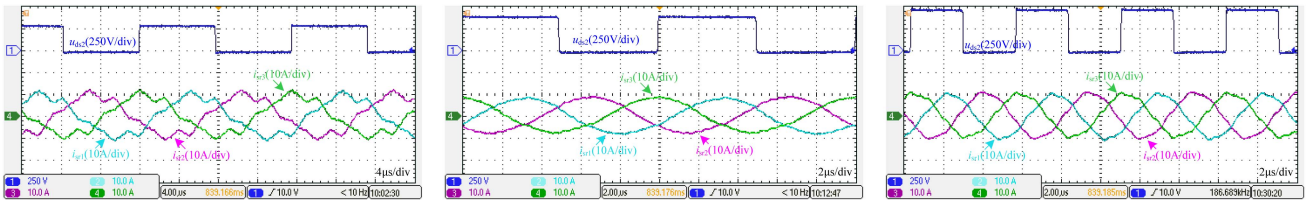

Fig. 19. Experimental waveforms of 3P-IL&PR mode in backward discharging operation i_{sr1}, i_{sr2}, i_{sr3}, and u_{ds2}. (a) When $V_S = 300$ V, $P_o = 2.1$ kW. (b) When $V_S = 400$ V, $P_o = 2.7$ kW. (c) When $V_S = 480$ V, $P_o = 3$ kW.

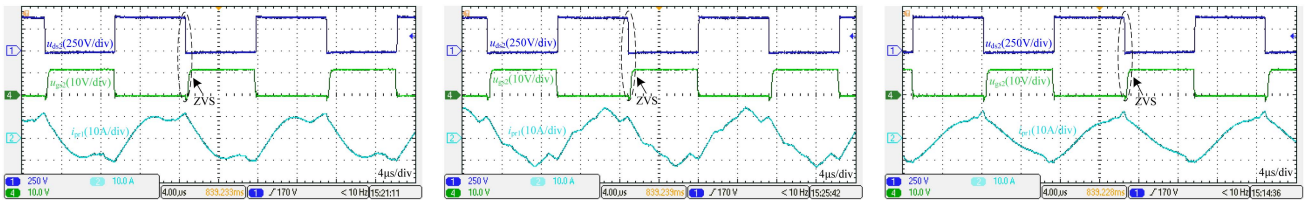

Fig. 20. Experimental waveforms in forward operation u_{ds2}, u_{gs2}, and i_{pr1} ($f_s < f_r$). (a) 1P-HB&PR mode. (b) 3P-IL&PR mode. (c) 2P-FB&PR mode.

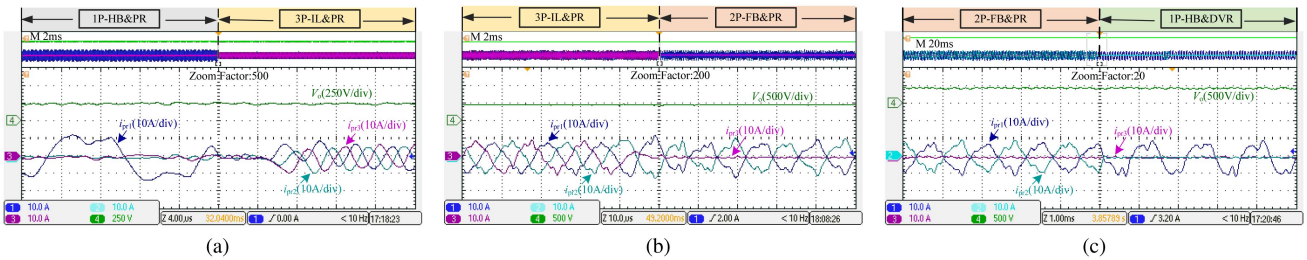

Fig. 21. Transition waveforms in forward operation. (a) 1P-HB&PR mode to 3P-IL&PR mode. (b) 3P-IL&PR mode to 2P-FB&PR mode. (c) 2P-FB&PR mode to 1P-HB&DVR mode.

During the floating-charging stage, improving the efficiency under light-load conditions is of great significance. The reason is that compared to other charging stages, the duration of this charging stage is much longer. Therefore, this will generate significant energy-saving effects over time. Fig. 18(i) shows the experimental waveforms.

B. Backward Discharging Stage

To protect the battery from excessive discharge, the converter only operates in 3P-IL&PR mode. The input voltage range of the mode is 300 V–480 V. The output power drops as the input voltage decreases. Owing to the three-phase interleaved structure, this mode also has more advantages in high-power applications. Fig. 19 shows the experimental waveforms in the backward mode, which demonstrate that the mode meets the design specifications for battery discharging at different power levels. Moreover, the three-phase resonant currents being in a balanced state, the converter is operating in good condition.

C. ZVS Condition

As shown in Fig. 20, the converter is capable of attaining ZVS in the single-phase, two-phase, and three-phase transmission paths. From Fig. 20(a), the driving voltage u_{gs2} starts to rise after the drain-source voltage u_{ds2} drops to zero, which indicates that the parasitic capacitor of the switch S_2 has discharged to zero and the resonant current i_{pr1} freewheels into the body diode of S_2. Thus, the ZVS condition is satisfied. The ZVS process of Fig. 20(b) and (c) is similar to that of Fig. 20(a). Since 1P-HB&DVR and 1P-HB&PR share the same conditions for soft switching, the converter can achieve ZVS in all four proposed modes.

D. Mode Transition

The transition waveforms of adjacent operating modes are shown in Fig. 21. The transition between 1P-HB&PR mode and 3P-IL&PR mode is triggered when $I_S = 4$ A, $V_S = 270$ V, which is shown in Fig. 21(a). When the output voltage of the converter rises to 270 V, the other two phases start working, and the single-phase resonant current gradually becomes the three-phase resonant currents.

The transition between 3P-IL&PR mode and 2P-FB&PR mode is triggered when $I_S = 3$ A, $V_S = 480$ V, as shown in Fig. 21(b). When the output current of the converter drops to 3 A, the phase-C is shed, and the three-phase resonant currents

TABLE II
COMPARISON OF THE PROPOSED CONVERTER AND EXISTING CONVERTERS

References	Converter in [9]	Converter in [14]	Converter in [24]	Converter in [25]	Converter in [27]	Proposed
DC bus voltage	400V	400V	380-420V	400V	400V	400V
Topology	1P-FB CLLC	1P-FB L-LLC	3P-IL CLLLC	3P-IL LLCL	3P-Multimode LLC	3P-Mulitimode CLLLC
Direction	Bidirectional	Bidirectional	Bidirectional	Bidirectional	Unidirectional	Bidirectional
Charging voltage V_S	250-450V	320-480V	280-420V	250-420V	32-100V	150-480V
Discharging voltage V_P	250-450V	320-480V	300-400V	300-420V	-	300-480V
Output power	1kW	1.6kW	3.3kW	3.3kW	3kW	3.3kW
Forward peak efficiency	97.9%	97.8%	97.2%	97.8%	96%	98%
Backward peak efficiency	98.06%	97.8%	96.9%	98%	-	98.1%
20% load	-	94%	93.8%	93%	94.2%	96%
Pre-charging	No	No	No	No	Yes	Yes

gradually become the two-phase resonant currents. The transition between 2P-FB&PR mode and 1P-HB&DVR mode is triggered when $I_S = 1.5$ A, $V_S = 480$ V, as illustrated in Fig. 21(c). Once the output current of the converter decreases to 1.5 A, phase-B is shed. Subsequently, the two-phase resonant currents gradually transform into the single-phase resonant currents.

The experimental results indicate that the transition between adjacent modes can be smoothly completed and is highly stable.

E. Analysis of Working Process and Efficiency Curves

The process of the CC charging stage and CV charging stage in forward operation is shown in Fig. 22(a). The whole process is divided into three stages, 4 A precharging, 6.9 A bulk-charging, and 480 V absorption-charging stage. In the whole CC charging stage, the efficiency of the prototype is above 94.5%. The maximum efficiency of 1P-HB&PR mode reaches 96.6%. The efficiency of the 3P-IL&PR mode is above 96% during most of the time, and the maximum efficiency reaches 98%.

When the CC charging stage is completed, the converter enters light-load charging at maximum output voltage. As illustrated in Fig. 22(b), the light-load charging stage is divided into an absorption-charging stage and a float-charging stage, corresponding to 2P-FB&PR mode and 1P-HB&DVR mode, respectively. Compared with 3P-IL&PR mode, the efficiency increases by about 1% at 1000 W, nearly 4% at 500 W, and almost 16% at 250 W. The results verify that the newly designed phase-shielding strategy greatly improves the light-load efficiency of the converter.

As shown in Fig. 23, the output power is configured to decrease as the input voltage U_S drops. This is done in order to maximize the utilization of the converter's power capacity during the backward discharging operation. For instance, when the input voltage U_S goes from 480 V to 400 V, the output power correspondingly decreases from 3 kW to 2.7 kW. In the whole process of backward operation, the efficiency is greater than 96.5% and the maximum efficiency reaches 98.1%. A comparison between the proposed improved 3P-multimode *CLLLC* resonant converter and existing converters is given in Table II. It can be observed that the proposed converter possesses excellent performance in voltage gain range, peak efficiency, and light-load efficiency. In addition, the converter possesses precharging mode for covering the recovery stage of battery.

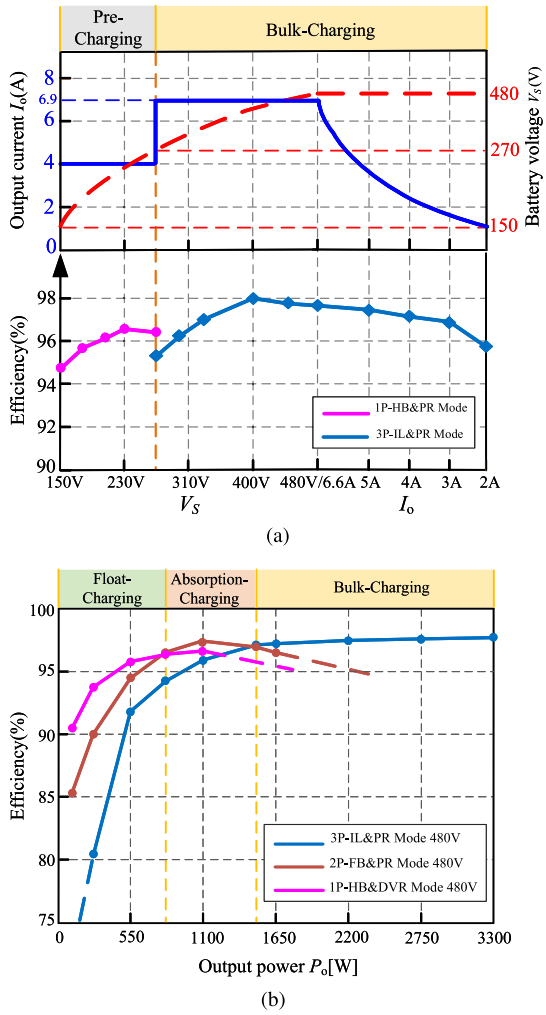

Fig. 22. Forward efficiency curves of the converter. (a) 1P-HB&PR mode and 3P-IL&PR mode. (b) Comparison of light-load efficiency.

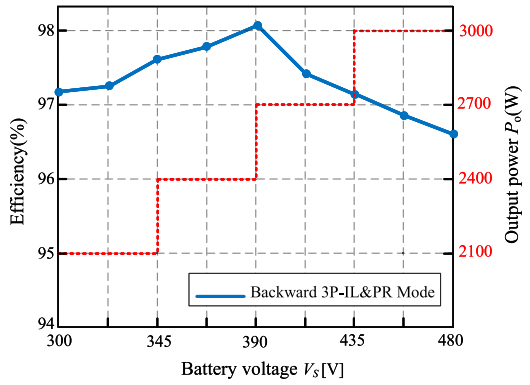

Fig. 23. Backward efficiency curves of the proposed converter.

VI. Conclusion

To address the problems of limited gain range and the inability to achieve high efficiency under light-load conditions in the conventional three-phase *CLLLC* resonant converter, this article proposes a modified multimode three-phase *CLLLC* bidirectional resonant converter with PFM control. Through the newly designed phase-shielding strategy, the converter incorporates precharging mode and float-charging mode, enabling it to cover all charging stages of the battery pack. The 1P-HB&PR mode offers a low gain range, facilitating the low-voltage and low-current required to restore a completely depleted battery. By implementing the 2P-FB&PR mode, the converter can achieve improved light-load efficiency Moreover, the 1P-HB&DVR mode can further enhance the light-load efficiency of the converter, making it suitable for the floating-charging stage. All the charging stages of the battery can be covered through the four operating modes. The experimental results confirm the benefits of the proposed phase-shedding strategies in terms of expanding the voltage gain range and significantly enhancing the light-load efficiency.

References

[1] S. Zou, J. Lu, A. Mallik, and A. Khaligh, "Modeling and optimization of an integrated transformer for electric vehicle on-board charger applications," *IEEE Trans. Transport. Electrific.*, vol. 4, no. 2, pp. 355–363, Jun. 2018.

[2] H. V. Nguyen, D.-C. Lee, and F. Blaabjerg, "A novel sic-based multifunctional onboard battery charger for plug-in electric vehicles," *IEEE Trans. Power Electron.*, vol. 36, no. 5, pp. 5635–5646, May 2021.

[3] Z. U. Zahid, Z. M. Dalala, R. Chen, B. Chen, and J. -S. Lai, "Design of bidirectional dc–dc resonant converter for vehicle-to-grid (V2G) applications," *IEEE Trans. Transp. Electrific*, vol. 1, no. 3, pp. 232–244, Oct. 2015.

[4] J. Jung, H. Kim, M. Ryu, and J. Baek, "Design methodology of bidirectional *CLLC* resonant converter for high-frequency isolation of dc distribution systems," *IEEE Trans. Power Electron.*, vol. 28, no. 4, pp. 1741–1755, Apr. 2013.

[5] Y.-E. Wu and Y.-T. Ke, "A novel bidirectional isolated dc-dc converter with high voltage gain and wide input voltage," *IEEE Trans. Power Electron.*, vol. 36, no. 7, pp. 7973–7985, Jul. 2021.

[6] M. Li, Z. Ouyang, and M. A. Andersen, "High-frequency *LLC* resonant converter with magnetic shunt integrated planar transformer," *IEEE Trans. Power Electron.*, vol. 34, no. 3, pp. 2405–2415, Mar. 2019.

[7] Y. Wei, Q. Luo, and A. Mantooth, "Overview of modulation strategies for *LLC* resonant converter," *IEEE Trans. Power Electron.*, vol. 35, no. 10, pp. 10423–10443, Oct. 2020.

[8] H. Li et al., "A bidirectional synchronous/asynchronous rectifier control for wide battery voltage range in SiC bidirectional *LLC* chargers," *IEEE Trans. Power Electron.*, vol. 37, no. 5, pp. 6090–6101, May 2022.

[9] J. Min and M. Ordonez, "Bidirectional resonant *CLLC* charger for wide battery voltage range: Asymmetric parameters methodology," *IEEE Trans. Power Electron.*, vol. 36, no. 6, pp. 6662–6673, Jun. 2021.

[10] A. Sankar, A. Mallik, and A. Khaligh, "Extended harmonics based phase tracking for synchronous rectification in *CLLC* converters," *IEEE Trans. Ind. Electron.*, vol. 66, no. 8, pp. 6592–6603, Aug. 2019.

[11] T. Zhu, F. Zhuo, F. Zhao, F. Wang, H. Yi, and T. Zhao, "Optimization of extended phase-shift control for full-bridge *CLLC* resonant converter with improved light-load efficiency," *IEEE Trans. Power Electron.*, vol. 35, no. 10, pp. 11129–11142, Oct. 2020.

[12] S. A. Ansari, J. N. Davidson, and M. P. Foster, "Fully-integrated transformer with asymmetric primary and secondary leakage inductances for a bidirectional resonant converter," *IEEE Trans. Ind. Appl.*, vol. 59, no. 3, pp. 3674–3685, May/Jun. 2023.

[13] S. Zong, G. Fan, and X. Yang, "Double voltage rectification modulation for bidirectional DC/DC resonant converters for wide voltage range operation," *IEEE Trans. Power Electron.*, vol. 34, no. 7, pp. 6510–6521, Jul. 2019.

[14] H. Wu, S. Ding, K. Sun, L. Zhang, Y. Li, and Y. Xing, "Bidirectional soft-switching series-resonant converter with simple PWM control and load-independent voltage-gain characteristics for energy storage system in dc microgrids," *IEEE J. Emerg. Sel. Topics Power Electron.*, vol. 5, no. 3, pp. 995–1007, Sep. 2017.

[15] J. Liu, Y. Ai, S. Chen, Z. Zhang, and Y. Shi, "A hybrid pulse frequency modulation control strategy for *L-LLC* resonant converter," *IEEE J Emerg Sel Top Power Electron.*, vol. 10, no. 6, pp. 6960–6972, Dec. 2022.

[16] Y. Zhang, D. Zhang, J. Li, and H. Zhu, "Bidirectional *LCLL* resonant converter with wide output voltage range," *IEEE Trans. Power Electron.*, vol. 35, no. 11, pp. 11813–11826, Nov. 2020.

[17] O. Kirshenboim and M. M. Peretz, "Combined multilevel and two-phase interleaved *LLC* converter with enhanced power processing characteristics and natural current sharing," *IEEE Trans. Power Electron.*, vol. 33, no. 7, pp. 5613–5620, Jul. 2018.

[18] H. Dong, X. Xie, S. Xu, and H. Yu, "A novel current sharing scheme for two-phase interleaved *LLC* converter based on virtual controllable voltage sources," *IEEE Trans. Power Electron.*, vol. 37, no. 2, pp. 1210–1216, Feb. 2022.

[19] G. Li, D. Yang, B. Zhou, Y. -F. Liu, and H. Zhang, "Integration of three-phase *LLC* resonant converter and full-bridge converter for hybrid modulated multioutput topology," *IEEE J. Emerg. Sel. Topics Power Electron.*, vol. 10, no. 5, pp. 5844–5856, Oct. 2022.

[20] R. Kumar, P. K. Behera, and M. Pattnaik, "A comparative analysis of two-phase and three-phase interleaved bidirectional DC-DC converter," in *Proc. 2023 IEEE Int. Students' Conf. Elect., Electron. Comput. Sci.*, Bhopal, India, 2023, pp. 1–5.

[21] C. Fei, R. Gadelrab, Q. Li, and F. C. Lee, "High-frequency three-phase interleaved *LLC* resonant converter with GaN devices and integrated planar magnetics," *IEEE J. Emerg. Sel. Topics Power Electron.*, vol. 7, no. 2, pp. 653–663, Jun. 2019.

[22] K. Zhou, Y. Huang, and S. Zheng, "Research on bidirectional on-board charging system based on three-phase wye-wye connected *CLLLC* resonant converter," *IEEE Access*, vol. 11, pp. 101998–102013, 2023.

[23] Q. Zhao, T. Wang, Y. Zheng, H. Ding, and D. Wang, "Three-phase *LLCL* bidirectional resonant converter with wide output voltage range," *IEEE Trans. Power Electron.*, vol. 39, no. 9, pp. 11244–11255, Sep. 2024.

[24] N. Shafiei, M. Ordonez, M. Craciun, C. Botting, and M. Edington, "Burst mode elimination in high-Power *LLC* resonant battery charger for electric vehicles," *IEEE Trans. Power Electron.*, vol. 31, no. 2, pp. 1173–1188, Feb. 2016.

[25] S. A. Arshadi, M. Ordonez, W. Eberle, M. Craciun, and C. Botting, "Three-phase *LLC* battery charger: Wide regulation and improved light-load operation," *IEEE Trans. Power Electron.*, vol. 36, no. 2, pp. 1519–1531, Feb. 2021.

[26] B. Li, Q. Li, and F. C. Lee, "Phase shading for light load efficiency improve in three-phase resonant converter with integrated PCB winding magnetics," in *Proc. 10th Int. Conf. Power Electron. ECCE Asia*, Busan, South Korea, 2019, pp. 2362–2367.

[27] A. M. Kamalkhani and E. Afjei, "A modified three-phase *LLC* resonant converter: Phase shedding and light-load operation suitable for welding applications," in *Proc. 9th Iranian Conf. Renewable Energy Distrib. Gener.*, Mashhad, Iran, 2022, pp. 1–8.

[28] F. Jin, A. Nabih, and Q. Li, "Light load efficiency improvement of three phase *CLLC* resonant converter for on-board charger applications," in *Proc. 2022 IEEE Appl. Power Electron. Conf. Expo.*, Houston, Texas, USA, 2022, pp. 1–7.

Tianrui Wang received the B.S. degree in electrical engineering and automation from Ningbo University of Technology, Ningbo, China, in 2022. He is currently working toward the M.S. degree in electrical engineering with Yanshan University, Qinhuangdao, China.

His main research interests include high-frequency switching mode converter and soft switching technology.

Qinglin Zhao received the B.S. degree in industrial automation from the Northeast Heavy Machinery College (which was renamed Yanshan University in 1997), Qiqihar, China, in 1992, and the M.S. and Ph.D. degrees in power electronics and power drives from Yanshan University, Qinhuangdao, China, in 2003 and 2007, respectively.

He is currently a Professor with the School of Electrical Engineering, Yanshan University. His research interests include high frequency and high efficiency power converters, and control of grid-connected inverters.

Hao Ding (Member, IEEE) received the B.S. and Ph.D. degrees in electrical engineering from Yanshan University, Qinhuangdao, China, in 2012 and 2017, respectively.

He is currently an Associate Professor with the Department of Electrical Engineering, Yanshan University. His current research interests include nonlinear and intelligent control for power converters and ac drives, stability and power quality of power-electronics-dominated power systems, high-power converters such as current source converter and modular multilevel converter.

Deyu Wang (Member, IEEE) received the M.S. and Ph.D. degrees in power electronics and power drives from Yanshan University, Qinhuangdao, China, in 2005 and 2009, respectively.

Since 2015, he has been an Associate Professor with the School of Electrical Engineering, Yanshan University. His main research interests include wireless power transfer technology, high-frequency switching mode converter, and solid-state pulsed power application.